

THE AGES AND MASSES OF LYMAN ALPHA GALAXIES AT $z \sim 4.5$ ¹

STEVEN L. FINKELSTEIN², JAMES E. RHOADS, SANGEETA MALHOTRA³, NORBERT PIRZKAL⁴ & JUNXIAN WANG⁵

¹ Observations reported here were obtained at the MMT Observatory, a joint facility of the University of Arizona and the Smithsonian Institution

² Department of Physics, Arizona State University, Tempe, AZ 85287

³ School of Earth and Space Exploration, Arizona State University, Tempe, AZ 85287

⁴ Space Telescope Science Institute, 3700 San Martin Drive, Baltimore, MD 21218 and

⁵ University of Science and Technology of China, Hefei, Anhui 230026, China

Draft version October 2, 2018

ABSTRACT

We examine the stellar populations of a sample of 98 $z \sim 4.5$ Lyman alpha emitting galaxies using their broadband colors derived from deep photometry at the MMT. These galaxies were selected by narrowband excess from the Large Area Lyman Alpha survey. Twenty-two galaxies are detected in two or more of our MMT filters (g', r', i' and z'). By comparing broad and narrowband colors of these galaxies to synthetic colors from stellar population models, we determine their ages and stellar masses. The highest equivalent width objects have an average age of 4 Myr, consistent with ongoing star formation. The lowest EW objects show an age of 40 - 200 Myr, consistent with the expectation that larger numbers of stars are causing low EWs. We found masses ranging from $2 \times 10^7 M_{\odot}$ for the youngest objects in the sample to $2 \times 10^9 M_{\odot}$ for the oldest. It is possible that dust effects could produce large equivalent widths even in older populations by allowing the Lyman alpha photons to escape, even while the continuum is extinguished, and we present models for this scenario also.

Subject headings: galaxies: fundamental parameters – galaxies: high-redshift – galaxies: ISM – galaxies: evolution

1. INTRODUCTION

There are two popular techniques for locating galaxies at high redshift: the Lyman Break technique (Steidel et al. 1996) and narrowband selection. The second entails observing a galaxy in a narrowband filter containing a redshifted emission line. This method is useful to select high redshift galaxies with strong Lyman alpha ($\text{Ly}\alpha$) emission lines. While the line emission properties of Lyman Break galaxies (LBGs) are known, little is known about the continuum properties of $\text{Ly}\alpha$ galaxies because they are so faint. Studying the continuum properties of these $\text{Ly}\alpha$ galaxies at high-redshift can tell us about their age, stellar mass, dust content and star formation history.

We have used the narrowband selection technique to locate and study Lyman alpha emitting galaxies (LAEs) at $z \sim 4.5$. Similar studies have been done both in this field and in other fields (e.g., Rhoads et al 2000, 2004; Rhoads & Malhotra 2001; Malhotra & Rhoads 2002; Cowie & Hu 1998; Hu et al 1998, 2002, 2004; Kudritzki et al 2000; Fynbo, Moller, & Thomsen 2001; Pentericci et al 2000; Stiavelli et al 2001; Ouchi et al 2001, 2003, 2004; Fujita et al 2003; Shimasaku et al 2003, 2006; Kodaira et al 2003; Ajiki et al 2004; Taniguchi et al 2005; Venemans et al 2002, 2004). In many of these studies, the strength of the Lyman alpha ($\text{Ly}\alpha$) line has been found to be much greater than that of a normal stellar population (Kudritzki et al. 2000; Dawson et al. 2004). Malhotra and Rhoads (2002; hereafter MR02) found numerous LAEs with rest frame equivalent widths (EWs) $> 200 \text{ \AA}$. Assuming a constant star formation rate, the EW of a normal stellar population will asymptote toward 80 \AA by 10^8 years, down from a maximum value of $\sim 240 \text{ \AA}$. These galaxies are of interest because it is believed that this strong $\text{Ly}\alpha$ emission is a sign of ongoing star

formation activity in these galaxies (Partridge & Peebles 1967), and it could mean that these are some of the youngest galaxies in the early universe.

There are a few possible scenarios that could be creating this large EW. Strong $\text{Ly}\alpha$ emission could be produced via star formation if the stellar photospheres are hotter than normal, which could happen in low metallicity galaxies. It could also mean that these galaxies have their stellar mass distributed via a top-heavy initial mass function (IMF). Both of these scenarios are possible in primitive galaxies, which are thought to contain young stars and little dust.

Active galactic nuclei also produce a large $\text{Ly}\alpha$ EW. In an optical spectroscopic survey of $z \sim 4.5$ $\text{Ly}\alpha$ galaxies, Dawson et al. (2004) found large $\text{Ly}\alpha$ equivalent widths, but narrow physical widths ($\Delta v < 500 \text{ km s}^{-1}$). They also placed tight upper limits on the flux of accompanying high-ionization state emission lines (e.g., NV $\lambda 1240$, SiIV $\lambda 1398$, CIV $\lambda 1549$ and HeII $\lambda 1640$), suggesting that the large $\text{Ly}\alpha$ EW is powered by star formation rather than AGN. Additionally, Type I (broad-lined) AGN are ruled out because the width of the $\text{Ly}\alpha$ line in such an object is greater than the width of the narrowband filters which were used (see Section 2.3). While Type II AGN lines are narrower than our filters, they remain broader than the typical line width of our $\text{Ly}\alpha$ sample as determined by followup spectroscopy (e.g., Rhoads et al. 2003). Malhotra et al. (2003) and Wang et al. (2004) searched for a correlation between LAEs and Type II AGN using deep *Chandra X-Ray Observatory* images. 101 $\text{Ly}\alpha$ emitters were known to lie in the two fields observed with *Chandra*, and none of them were detected at the 3σ level ($L_{2-8keV} = 2.8 \times 10^{42} \text{ ergs s}^{-1}$). The sources remained undetected when they were stacked, and they concluded that less than 4.8% of the $\text{Ly}\alpha$ emit-

ters they studied could be possible AGNs. Therefore, we are confident that there are at most a few AGN in our Ly α galaxy sample.

Another possible scenario involves enhancement of the Ly α line in a clumpy medium. In this scenario, the continuum light is attenuated by dust whereas the Ly α line is not, resulting in a greatly enhanced observed Ly α EW (Neufeld 1991; Hansen & Oh 2006). This can happen if the dust is primarily in cold, neutral clouds, whereas the inter-cloud medium is hot and mainly ionized. Because Ly α photons are resonantly scattered, they are preferentially absorbed at the surface. Thus it is highly unlikely that a Ly α photon will penetrate deep into one of these clouds. They will be absorbed and re-emitted right at the surface, effectively scattering off of the clouds and spending the majority of their time in the inter-cloud medium. However, continuum photons are not resonantly scattered, and if the covering factor of clouds is large, they will in general pass through the interior of one. Thus the continuum photons will suffer greater attenuation than the Ly α photons, effectively enhancing the Ly α EW.

These Ly α galaxies are so faint compared to other high- z objects that have been studied, that not a lot is known about their continuum properties. Our primary goal is to better constrain the ages and stellar masses of these objects from their continuum light in order to better understand the driving force behind the strength of the Ly α line. We have obtained deep broadband images in the g' , r' , i' and z' bands for this purpose. Using the colors of these galaxies, we can study continuum properties of individual Ly α emitting galaxies at this redshift for the first time, allowing us to estimate their age, mass, star formation rate and dust content. The next phase of our project will be to look into the likelihood of dust causing the large Ly α EW, which we will begin to do in this paper, as the colors of these galaxies might distinguish the cause of the large EW. Blue colors would indicate young stars with hot photospheres, while red colors would indicate dust quenching of the continuum, enhancing the Ly α EW. Observations, data reduction technique and sample selection are reported in Section 2; results are presented in Section 3, and they are discussed in Section 4. Conclusions are presented in Section 5.

2. DATA HANDLING

2.1. Observations

The Large Area Lyman Alpha (LALA) survey began in 1998 using the 4m Mayall telescope at the Kitt Peak National Observatory (KPNO). The final area of this survey was 0.72 deg^2 in two fields, Boötes and Cetus, centered at $14^{\text{h}}25^{\text{m}}57^{\text{s}}$, $+35^{\circ}32'$ (J2000) and $02^{\text{h}}05^{\text{m}}20^{\text{s}}$, $-04^{\circ}55'$ (J2000) respectively (Rhoads et al. 2000). The LALA survey found large samples of Ly α emitting galaxies at $z = 4.5, 5.7$ and 6.5 , with a spectroscopic success rate of up to 70%. We observed the LALA Cetus Field for three full nights in 2005 November, and again for four 1/4 nights in 2006 January, using the Megacam instrument (McLeod et al. 1998) at the Multiple Mirror Telescope (MMT). Megacam is a large mosaic CCD camera with a $24' \times 24'$ field of view, made up of 36 CCDs with 2048×4608 pixels. Each pixel is $0''.08$ on the sky. We acquired deep broadband images in four Sloan Digital Sky Survey (SDSS) filters: g' , r' , i' and z' . The total expo-

sure time in the g' , r' , i' and z' filters were 4.33, 3.50, 4.78 and 5.33 hours respectively. Given that the seeing during the run was rarely below $0''.8$, we chose to bin the pixels 2×2 to reduce data volume, resulting in a final pixel scale of $\sim 0''.16$ per pixel in our individual images.

2.2. Data Reduction

The data were reduced in IRAF¹ (Tody 1986, 1993), using the MSCRED (Valdes & Tody 1998; Valdes 1998) and MEGARED (McLeod et al. 2006) reduction packages. The data were first processed using the standard CCD reduction steps done by the task `ccdproc` (overscan correction, trim, bias subtraction and flat fielding). Bad pixels were flagged using the Megacam bad pixel masks included with the MEGARED package.

Fringing was present in the i' and z' band data, and needed to be removed. For this, we made object masks using the task `objmasks`². We then took a set of science frames in each filter, and combined them to make a skyflat using `sflatcombine` (using the object masks to exclude any objects from the resultant image). This skyflat was then median smoothed on a scale of 150×150 pixels (i') and 200×200 pixels (z'). The smoothed images were subtracted from the unsmoothed images, and the result was a fringe frame for each band. The fringing was then removed from the science images using the task `rmfringe`, which scales and subtracts the fringe frame. To make the illumination correction, skyflats were made, median smoothed 5×5 pixels, normalized and divided out of the science images.

The amplifiers in the reduced images were merged (from 72 to 36 extensions) using the MEGARED task `megamerge`. The WCS written in the image header at the telescope is systematically off by 0.5 degrees in rotation, so we used the task `fixmosaic` to adjust the rotation angle so that the WCS solution works better. The WCS was then determined using `megawcs`, and the WCS distortion terms were installed in the header using the task `zpn`.

The 36 chips were combined into a single extension using the program `SWarp`³. We ran `SWarp` on each input image, using a corresponding weight map which gave zero weight to known bad pixels and cosmic ray hits. We located the cosmic rays using the method of Rhoads (2000). We specified the center of the output images to be the average center of the five dither positions we used ($02^{\text{h}}04^{\text{m}}56^{\text{s}}$, $-05^{\circ}01'01''$ J2000), which corresponded to an image size of 11988×10881 pixels and a pixel scale of $0''.1587$ per pixel. During this process, each image was resampled (using the Lanczos-3 6-tap filter) and interpolated onto the new pixel grid. While this was done, `SWarp` determined and subtracted the background value in each extension.

¹ IRAF is distributed by the National Optical Astronomy Observatories (NOAO), which is operated by the Association of Universities for Research in Astronomy, Inc. (AURA) under cooperative agreement with the National Science Foundation.

² In order to prevent fringing from making it onto the object masks, we first made a skyflat without object masks, and divided this skyflat out of the science data. We then got the object masks from these quasi-fringe removed images. The rest of the procedure used the untouched science frames.

³ `SWarp` is a program that resamples and co-adds together FITS images, authored by Emmanuel Bertin. It is distributed by Terapix at: <http://terapix.iap.fr/soft/swarp>.

An initial stack for each filter was made using SWarp to average together the individual images. To make the final version of the stack, we needed to remove the satellite trails which littered our images. To do this, we created a difference image between each individual input image and the initial stack. Using a thresholding technique, we flagged the satellite trails in this image, and combined those flags with the existing weight-maps. We ran SWarp a final time with this as the input weight map, creating the final stack. We did this process for each band, giving us four images, one final stack in each of the g' , r' , i' and z' bands. In an attempt to increase the signal of our objects, we tried co-adding R and I band images from the NOAO Deep Wide-Field Survey (NDWFS)(Jannuzi & Dey 1999) to our r' and i' images, however the additional signal did not make a significant difference in the results.

To calculate the photometric zeropoint for our observations we took images of the standard stars SA95 190 and SA95 193 during our run, where the zeropoint is defined as the magnitude of an object with one count in the image (for an integration time of 400s). These standard stars are from Landolt (1992), and we used the transforms from Johnson-Morgan-Cousins to SDSS magnitudes from Fukugita et al. (1996). Averaging the results from the two stars for each band, we obtained these zeropoints: $g'=33.13$, $r'=33.00$, $i'=32.58$ and $z'=31.43$. Using these zeropoints with our data, all of our results are in AB magnitudes⁴.

2.3. Lyman α Galaxy Selection

To extract the objects from each stack, we used the SExtractor package (Bertin & Arnouts 1996). For SExtractor to accurately estimate the errors in the flux, it needed to know the gain in the input images. To calculate this, we needed the mean and standard deviation of the background of the images. Because the background was subtracted out in SWarp, we obtained the average background value in each band by averaging the values obtained from the pre-SWarp images, and adding this value onto the final stacks. We then ran SExtractor in the two-image mode using a nine pixel aperture ($2.''32$) with the narrowband images from the LALA survey, giving us catalogs of objects which were detected in both images.

The method we have used to locate Ly α galaxies involves taking an image using a narrowband filter containing the wavelength for Ly α at a certain redshift. We used the catalog from MR02, which was based on LALA narrowband images and broad band B_w , R , and I data from the NDWFS (Jannuzi & Dey 1999). The narrowband data consists of five overlapping narrowband filters, each with a FWHM $\sim 80\text{\AA}$. The central wavelengths are $\lambda\lambda 6559$ (H0), 6611 (H4), 6650 (H8), 6692 (H12) and 6730 (H16), giving a total redshift coverage $4.37 < z < 4.57$. To ensure that there was no overlap, we only used objects selected from the H0, H8 and H16 filters in our analysis. In order to compare the two data sets, the Megacam data were registered and remapped onto the same scale as the narrowband data using the IRAF tasks `wcsmmap` and `geotran`.

Selection criteria for the MR02 catalog, following

⁴ For more details on our reduction and analysis process, see: <http://stevnf.asu.edu/Reduction.html>

Rhoads & Malhotra 2001, were as follows: (1) 5σ significance detection in the narrowband: This is calculated using an SExtractor aperture flux with the associated flux error; $\text{flux/error} \geq 5$. (2) 4σ significant excess of narrowband flux: This was calculated by taking narrowband flux - broadband flux, both calibrated in physical units, and the associated error ($\sqrt{\text{error}_{\text{broad}}^2 + \text{error}_{\text{narrow}}^2}$) and demanding that $\text{flux difference} / \text{error} \geq 4$. (3) Factor of ≥ 2 ratio between broad and narrow band fluxes, calibrated to the same units. (4) No more than 2σ significant flux in the bluest filter observed (B_w).

2.4. Stellar Population Models

In order to study the properties of the galaxies in our sample we compare them to stellar population models, using the stellar population modeling software by Bruzual & Charlot (2003). With these models, we were able to choose a range of ages, metallicities and star formation rates for comparison with our sample. We chose ages ranging from $10^6 - 10^9$ years, metallicities from $0.02 Z_{\odot} - Z_{\odot}$ and exponentially decaying star formation rates with a characteristic time-scale of $\tau = 10^3 - 2 \times 10^9$ years. We included dust via the Calzetti dust extinction law (Calzetti et al. 1994), which is applicable to starburst galaxies, in the range: $A_{1200} = 0 - 2$. Lastly, we included intergalactic medium (IGM) absorption via the prescription of Madau (1995).

The Bruzual & Charlot code (BC03) output the flux of a given stellar population in units of $L_{\odot} \text{\AA}^{-1}$. In order to go from flux in these units to bandpass averaged fluxes, we used the method outlined by Papovich et al. (2001). In short, we took the output from BC03, and converted it from f_{λ} into f_{ν} (units of $\text{erg s}^{-1} \text{cm}^{-2} \text{Hz}^{-1}$). This flux was then multiplied by the transmission function for a given bandpass, and integrated over all frequency. The bandpass averaged flux $\langle f_{\nu} \rangle$ is this result normalized to the integral of the transmission function. AB magnitudes (Oke & Gunn 1983) for the candidates were then computed.

In order to calculate colors which we could directly compare to our observations, it was necessary to add in emission line flux from the Ly α line, which appears in the r' filter at $z \sim 4.5$. While the BC03 software does not calculate emission line strengths, we were able to use one of its many other output quantities: the number of ionizing photons. We calculated the Ly α emission line strength (in units of $L_{\odot} \text{\AA}^{-1}$ to match the model output) by using:

$$\text{Ly}\alpha \text{ Linestrength} = \frac{hc}{\lambda_{\text{Ly}\alpha} L_{\odot} \Delta\lambda} \times \frac{2}{3} \times n_{\text{ion}} \quad (1)$$

where n_{ion} is the number of ionizing photons, $\Delta\lambda$ is the bin size of the wavelength array (1\AA), and the factor of $2/3$ represents the fraction of ionizing photons which will produce Ly α photons when interacting with the local interstellar medium (ISM) under Case B recombination⁵. In order to model the clumpy dust scenario, we needed to ensure that the Ly α line did not suffer dust attenuation. To do this, the continuum flux was multiplied by the Calzetti dust law before we added in the Ly α flux to the

⁵ This calculation follows the simple assumptions that no ionizing photons escape, and that all Ly α photons escape.

spectrum at the correct wavelength bin. In this case, the continuum suffers dust attenuation while the Ly α line does not.

3. RESULTS

3.1. Ly α Galaxy Candidates

Using the catalog described above, we have identified 98 objects as Ly α galaxy candidates within the 24' \times 24' Megacam field of view. We have classified 22 of these objects as continuum detections on the basis that they have at least 2σ detections in two of the r' , i' or z' bands (the other 76 objects were undetected at this level in the broadband data, but we stacked their fluxes for analysis).

We have in our possession IMACS spectra of objects in the LALA Cetus Field (Wang et al. 2007). These spectra have been used to identify the redshift of the Ly α line in these galaxies. Out of the 98 total Ly α galaxy candidates, 28 have been spectroscopically confirmed as being Ly α emitters at $z \sim 4.5$. Seven of these confirmations are among the 22 Megacam detections. Another seven of the Megacam detections have IMACS spectra but had no strong Ly α line identified, however some of these may show a line with deeper spectra.

3.2. Equivalent Width Distribution

We calculated the rest-frame equivalent widths of our 22 detections using the ratio of the line flux to the continuum flux via:

$$EW = \left(\frac{1 - \eta}{\frac{\eta}{\Delta\lambda_{BB}} - \frac{1}{\Delta\lambda_{NB}}} \right) \times (1 + z)^{-1} \quad (2)$$

where η is the ratio of narrowband to broadband flux (in units of f_ν), and the $\Delta\lambda$ s are the filter widths (80Å and 1220Å for the narrow and broad filters respectively). The narrowband fluxes are measured from the LALA narrowband data discussed above, and the broadband fluxes are measured from our MMT r' data.

Figure 1 shows the calculated rest-frame EWs of our 22 continuum detected galaxies. The range of EWs is 5 – 800Å⁶. While the range of our EW distribution peaks at the low end of previous studies (i.e. most of our objects have rest-frame EW $\lesssim 200$ Å), we recognize that the 76 undetected objects would all lie at the high EW end of this plot (in fact, they peak at EW well over 200Å). Because they are undetected, this means that their broadband fluxes were too faint to be detected in our survey. However, they still have very bright narrowband fluxes, indicating strong Ly α emission. This strong emission, coupled with faint broadband r' magnitudes, results in a high Ly α EW.

From models of normal stellar populations (those with a near-Solar metallicity and a Salpeter IMF), it was found that the maximum EW a galaxy could have is ~ 240 Å at $t \sim 10^6$ yr, with the EW approaching a steady value of 80Å at $t \sim 10^8$ yr (MR02; Charlot & Fall 1993). Our data show many objects with a rest-frame EW greater than 100Å. While individual galaxies

with EW this high are possible from normal stellar populations, the ratio of high-low EWs is much greater than it ought to be when we account for the 76 objects without MMT detections. This implies that something is causing the EW to be higher than normal. One of our goals in this study is to investigate whether the cause is massive stars creating more Ly α photons, or dust suppressing the continuum and thus enhancing the Ly α EW.

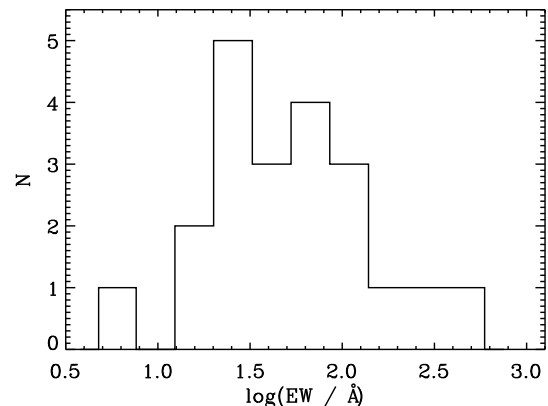


FIG. 1.— The distribution of rest-frame Ly α equivalent widths from our 22 detections. The EWs range from 5 – 800 Å. The single object with EW < 20 Å is likely an interloper that has managed to satisfy our selection criteria. A normal stellar population has an EW that asymptotes toward ~ 80 Å as its age goes to 10^8 years, so something is causing the Ly α EW of many of these objects to be higher..

We note that four objects among our MMT detections show observed equivalent width in excess of 230Å. Such high equivalent widths might be explained by a combination of extreme youth and/or low metallicity (e.g. Malhotra & Rhoads 2004), or might be produced by radiative transfer effects (Neufeld 1991, Hansen & Oh 2006). However, two of these objects are consistent with 200Å equivalent width at the 1σ level, and the other two at the 2σ level, so such mechanisms are not strictly required to explain these objects. Stronger evidence for such effects may be found among the 76 sources whose continuum emission was too faint for our MMT data.

3.3. Stacking Analysis

Our goal has been to be able to compare our objects to the models to obtain estimates of physical parameters such as age and stellar mass, along with dust content. We divided our objects into six groups which we then stacked (in order to damp down the errors) to get composite fluxes which we could compare to the models. The groups are: non-detections, which consists of the 76 selected objects which did not have a 2σ detection in at least two bands (out of r' , i' and z'); low EW, which consists of the seven detected objects with EW of 20–40Å; middle EW, which consists of the seven detected objects with EW of 45–100Å; high EW, which consists of the seven detected objects with EW ≥ 110 Å; detections, which consists of the 21 objects which were detected in the Megacam data; spectroscopically confirmed, which consists of the 28 objects (7 detected) which were confirmed to be Ly α emitters at $z \sim 4.5$. These stacks are

⁶ However, the object with an EW of 5 Å is likely an interloper. It has an $\sim 10\sigma$ detection in g' , and $> 30\sigma$ detections in r' , i' and z' . We will exclude this object from the rest of our analysis, giving us 21 detections.

shown in Figure 2.

3.4. Age and Mass Estimates

In order to study these galaxies, we have created numerous synthetic stellar population models which we compare to our observed galaxies. The most illuminating way in which we can study the observed vs. model galaxies are in a color-color plot (Figures 2 and 3). We have plotted the $r' - i'$ color vs. the $r' - nb$ color of our objects, and then overplotted many model curves. Because changing the metallicity did not much change the position of the model curves in the plane we are studying, we have elected to only use models with $Z = .02 Z_{\odot}$. The differing line styles represent the two different star formation rates we used, with the solid lines representing continuous star formation, and the dashed lines representing exponentially decaying star formation with a decay time of $\tau = 10^7$ years.

We ran the models at 24 different ages ranging from 1 Myr - 2 Gyr⁷, and in the figure we show the five ages which best surround the data, represented by different colors. We included dust in the models, ranging from $A_{1200} = 0 - 2$. The extent of the model tracks represents the different dust optical depths. As we discussed above, this dust does not affect the strength of the model Ly α line. We have connected the zero-dust end of the model tracks with the dotted black line in order to show where galaxies with no dust should lie.

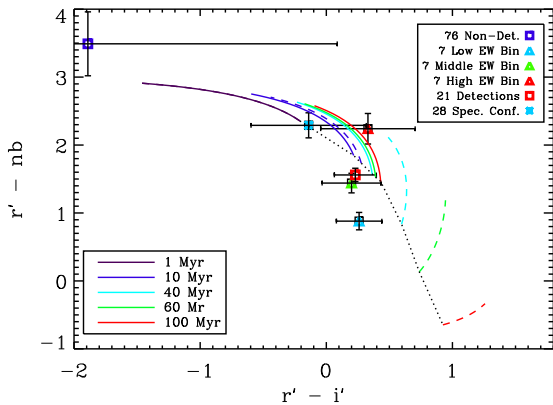


FIG. 2.— Color-color plot showing the six stacked points along with stellar population model tracks. The vertical axis is the $r' - nb$ color, and the horizontal axis is the $r' - i'$ color. The model tracks shown represent the colors of models in this plane. All models are for $.02 Z_{\odot}$. The solid tracks denote continuous star formation, while the dashed tracks denote exponentially decaying star formation, with a decay time of $\tau = 10^7$ years. The different colors of the model curves represent the ages of the models. The length of the model curves represent the model colors with differing amounts of dust. Models were run with $A_{1200} = 0 - 2$, with the A_{1200} point lying at the smallest $r' - nb$ color. The dotted black line connects the bottom of the model curves, and as such is the “zero-dust” line. Ages were found for each stack by minimizing the distance from the stack to the nearest $A_{1200} = 0$ model point (i.e. nearest point on the zero-dust line) for each star formation rate (20 different possible ages were used).

With significant flux in only three broadband points

⁷ At 1 Myr, the two different star formation rates have identical colors, so their model tracks overlap, that is why it appears as if there is no curve for an exponentially decaying galaxy at 1 Myr.

(r' , i' and z'), it would be hard to fit each stack to models with a full range of every parameter. However, given what we have learned from studying these objects in the color-color plane, it is relatively straightforward to fit an age to each of these stacks (assuming a star formation history and no dust). In order to fit the age, we considered 20 different ages ranging from 1 Myr - 200 Myr (including the five ages shown in Figure 2). By finding the model point (we used the $A_{1200} = 0$ point for each model; see discussion for details) closest to each stack, we have effectively found the average age of an object in the stack. Because we didn’t want to limit ourselves to one star formation history, we have found two ages for each object; one from the closest model with a constant star formation rate (SFR), and one from the closest model with an exponential SFR. These ages are reported in Tables 1 and 2 for constant and exponentially decaying SFR respectively. For a constant SFR, the ages ranged from 1 - 200 Myr, while for an exponentially decaying SFR, they ranged from 1 - 40 Myr.

In order to find the stellar mass, we wanted to only use the best-fit model for each stack. We took that to be the model with the best-fit age found above, and we calculated a mass for each SFR. The mass was found by a simple weighted ratio of object flux to model flux. We derived the weighting by minimizing the ratio of the mass error to the mass. The mass error was calculated via a monte carlo simulation using the flux errors from each band for each stack. These mass estimates are reported in Tables 1 and 2. The masses of the objects from both types of star formation rates range from $\sim 2 \times 10^7 - 2 \times 10^9 M_{\odot}$. These masses are indicative of an average object of the stack, and likewise the reported error is the error in the mean of the object mass in each stack, rather than the error in the measurement.

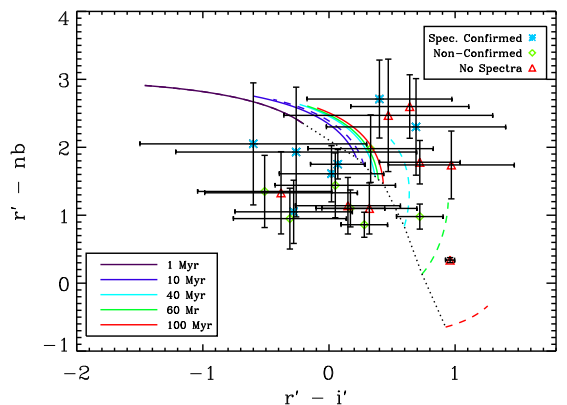


FIG. 3.— Color-color plot showing the location of the 21 individual detections (along with the outlier), along with stellar population model tracks. The individual galaxies are plotted with different colored symbols to denote whether they have been spectroscopically confirmed to be at $z \sim 4.5$. The axes and model tracks are the same as in Figure 2. In general, objects above the zero-dust line would have their EW enhanced due to dust effects, while objects below this line would have intrinsically high EWs, or have their whole spectrum attenuated by a geometrically homogeneous dust distribution (for the low EW subsample).

In Figure 3, we have plotted the 21 individually detected galaxies (plus the one outlier), along with their

TABLE 1
BEST-FIT AGES AND MASSES FOR A CONSTANT SFR

Stack	r' mag. of stack	Age (Myr)	χ^2	Mass ($10^8 M_\odot$) per object
7 Low EW	23.27±0.10	200	18.48	23.54±1.66
7 Mid EW	23.49±0.12	80	0.93	8.52±0.74
7 High EW	24.08±0.21	4	0.94	0.95±0.15
21 Det.	22.39±0.09	40	0.62	4.60±0.29
76 Undet.	23.31±0.47	1	6.59	0.19±0.07
28 Spec. Conf.	22.96±0.18	3	0.05	0.62±0.09

NOTE. — Each model has a metallicity of $.02 Z_\odot$. The low EW bin is from 20–40 Å; the middle bin is from 45–100 Å; the highest bin has objects with $EW \geq 110$ Å. The bin with 21 detected objects consists of the 21 galaxies which were detected at the 2σ level in at least two of the r' , i' or z' bands. The last bin consists of the 28 objects which were spectroscopically confirmed to have a Ly α line at $z \sim 4.5$. The χ^2 is defined as the square of the distance in sigma units to the best-fit age point (See Figure 2). The r' magnitude is for the stack as a whole, while the mass is per object.

1σ error bars. We have distinguished between the individual galaxies in order to show those that were spectroscopically confirmed. By their position in this plot, we hope to find out whether they have an intrinsically strong Ly α line, or one that is enhanced due to dust effects.

4. DISCUSSION

4.1. Age and Mass Estimates

We fitted the ages of our stacked points using dust-free models. Objects in the stack of the 76 non-detections have the lowest age by far of all of the stacks (1 Myr), and thus the lowest mass ($0.19 \times 10^8 M_\odot$). This is not surprising, however, because these objects are selected based on their Ly α line strength. In these galaxies, the line is strong enough to be seen clearly but the continuum is not, so they are intrinsically faint galaxies, implying a low stellar mass. Their colors are best fit by a low age, which also points to a low mass; the galaxy has simply not had that much time to form stars.

The three equivalent width bins show a logical trend in age and mass. The lowest EW bin has the highest age at 200 (40) Myr, and thus the highest mass at 23.54 (16.15) $\times 10^8 M_\odot$ for a continuous (exponentially decaying) SFR. This age is consistent with the fact that the EWs in this bin were not higher than normal, and thus this EW bin is best fit by an older stellar population. The middle EW bin has a younger age and a smaller mass, and the highest EW bin has the youngest age out of the three bins at 4 (4) Myr, with the smallest mass at 0.95 (0.94) $\times 10^8 M_\odot$. This would indicate that the objects with the highest EW are truly the most young and primitive galaxies in our sample (that were detected). The results for the stack of all 21 MMT-detected objects are intermediate among the results grouped by equivalent width, as expected. The ages for this stack were 40 (10) Myr, and masses were 4.6 (2.0) $\times 10^8 M_\odot$. The stack of spectroscopically confirmed objects should lie somewhere between the detected and non-detected stacks, and indeed this is the case, with ages of 3 (2) Myr, and masses of 0.62 (0.68) $\times 10^8 M_\odot$.

The overall mass range we found of $\sim 2 \times 10^7 - 2 \times 10^9$

TABLE 2
BEST-FIT AGES AND MASSES FOR AN EXPONENTIALLY
DECAYING SFR

Stack	Age (Myr)	χ^2	Mass ($10^8 M_\odot$) per object
7 Low EW Objects	40	4.05	16.15±1.14
7 Mid EW Objects	20	1.05	4.24±0.37
7 High EW Objects	4	0.97	0.94±0.14
21 Det. Objects	10	3.43	1.97±0.13
76 Undet. Objects	1	6.59	0.19±0.07
28 Spec. Conf. Objects	2	0.09	0.68±0.10

NOTE. — See Table 1 notes.

M_\odot is comparable to other studies of similar objects. Due to the fact that our observed magnitudes are brighter than the majority of surveys which we can compare to, we point to the trend between apparent magnitude and mass. That is, that the fainter an object is, the less massive it ought to be (assuming they are at similar redshifts). Ellis et al. (2001) discovered a very faint ($I \sim 30$) Ly α emitting galaxy at $z = 5.576$ that was able to be detected because it was lensed by a foreground galaxy. Due to its faint magnitude, this object was determined to have a mass of around $10^6 M_\odot$, implying a very young age (~ 2 Myr). This object is consistent with our results, in that it is both much fainter and much less massive than the objects we are studying in this paper. Gawiser et al. (2006) studied numerous LAEs which they detected at $z \sim 3.1$, with a median R magnitude of ~ 27 . In order to take advantage of the full spectral range available to them, they stacked their sources before performing SED fitting. When this was done, they found an average mass per object of $\sim 5 \times 10^8 M_\odot$. All of our stacks (except the stack of undetected objects) have an average individual object r' magnitude of less than 27, so even given the differences in photometric systems, they are likely brighter (much brighter in fact, due to their increased distance). While (depending on the SFR) not all of these stacks have masses higher than $5 \times 10^8 M_\odot$, they are of the same order.

Perhaps the best comparison to our results comes from the study by Pirzkal et al. (2007), where they are studying the properties of $z \sim 5$ LAEs detected in the GRISM ACS Program for Extragalactic Science (GRAPES) survey (Pirzkal et al. 2004). Using models with an exponentially decaying SFR, they found a mass range of $3 \times 10^6 - 3 \times 10^8 M_\odot$ in objects with an i' range of 25.52 – 29.35 (the i' range of an average object in our stacks is from 25.12 – 29.90). While the majority of our objects have i' brighter than 26 (all except objects from the undetected stack and the spectroscopically confirmed stack), all of the GRAPES objects except one have i' fainter than 26. This explains well the fact that our derived masses are in general greater than those derived for the GRAPES LAEs. We are studying intrinsically brighter, and thus more massive objects. While our wavelength baseline is not very large, we are able to estimate the mass of stars producing UV and Ly α light.

4.2. Dusty Scenario

In studying Figure 3, we have identified three distinct regions in the color-color plane: one region which would

house intrinsically blue objects, one region of red objects with high EW, and one of red objects with low EW. The region that lies below the zero-dust line and blueward of $r' - i' = 0$ would appear to house objects that have moderate-to-high EWs with blue colors, indicating that they are intrinsically blue, containing young stars. The lower EW/redder $r' - i'$ color sub-area of this region would contain objects may have some dust, but it is affecting both the continuum and Ly α line, lowering the EW and reddening the color.

The second region consists of the area above the zero-dust line with an $r' - nb$ color $\gtrsim 2$. This region would hold objects that lie in the dusty regime of the models, yet they would still have “red” $r' - nb$ colors, indicating a large EW. Objects such as these could be explained by dust quenching of the continuum (causing the red $r' - i'$ color), while the Ly α line would not be affected by the dust, making it appear to be strong (causing the red $r' - nb$ color). The last region consists of the area above the zero dust line, but with a smaller $r' - nb$ color ($r' - i' \sim 1$, $r' - nb = 1 - 1.5$). Objects in this area would have a redder $r' - i'$ color, with a smaller $r' - nb$ color (smaller EW), indicating that they are perhaps older galaxies with some dust effects present.

In the above paragraph, we have outlined different regions in our color-color plane which would house objects from the different scenarios we are examining. We plan to use this to determine the likelihood of dust quenching of the continuum resulting in a large Ly α EW. However, the current error bars on individual objects are large compared to their distance from the zero-dust line. In order to quantify this, we calculated the distance of each object from the zero-dust line in units of σ . The mean distance of the 21 objects we are studying is $1.10 \pm 0.48 \sigma$. While it is possible that the dust enhancement of the Ly α line is present in our sample, due to the large error bars we cannot rule out the possibility that all of these objects lie on the zero-dust line at a level of $\sim 1 \sigma$.

Performing the same exercise with the six stacked points with their smaller error bars, the mean distance from the zero-dust line is $1.17 \pm 0.81 \sigma$. However, the smaller error bars do allow us to make more of a characterization of a few of the stacks. We can most likely rule out clumpy dust enhancement of the Ly α line for the low and middle EW stacks, mainly because they lie below the zero-dust line, and far from the region in our color-color plane where we would expect to find the enhanced line. Also, in the line enhancement scenario, one would expect to find extremely high EW Ly α lines, and these two stacks do not contain the highest 33% EW ob-

jects in our sample. There still may be dust present in these objects, but it would be in a uniform distribution, quenching both the continuum and the Ly α line.

5. CONCLUSION

We have used MMT/Megacam broadband photometry in order to study the continuum properties of Ly α emitting galaxies at $z \sim 4.5$. By dividing our objects into six different categories and stacking them, we were able to derive age and stellar mass estimates for an average galaxy in each stack (ignoring dust effects). In all cases, the best fit ages were young, with the oldest age coming from objects with the lowest equivalent width. Even those objects had an age of only 200 Myr (40 Myr) for a continuous (exponentially decaying) star formation rate. As would be expected, the bin with the highest EW had the youngest age out of the continuum detected objects at 4 Myr (from both SFRs). The youngest age from both SFRs came from objects whose continuum flux was undetected, mostly because these were detected in the narrowband image, and not in the continuum images.

The derived stellar masses ranged from $\sim 2 \times 10^7 M_{\odot}$ for the undetected objects to $\sim 2 \times 10^9$ for the lowest EW objects. Our derived masses are consistent with other mass estimates of similar objects. In the majority of cases, the masses of our objects were greater than those from other studies (Ellis et al. 2001; Gawiser et al. 2006; Pirzkal et al. 2007). However, the magnitudes of our individual objects were brighter than those of the comparison studies, implying that our objects are larger, more massive galaxies than those from the other studies. In conclusion, while we have not yet been able to definitively determine the likelihood of dust enhancement of the Ly α line, we have been able to shed some light on the physical properties of these high- z objects. The Ly α galaxies in this survey, especially those with the largest Ly α EW, are some of the youngest and least-massive objects in the early universe known to date.

This work was supported by the Arizona State University/NASA Space Grant, the ASU Department of Physics and the ASU School of Earth and Space Exploration. This work made use of images and/or data products provided by the NOAO Deep Wide-Field Survey (Jannuzi and Dey 1999), which is supported by the National Optical Astronomy Observatory (NOAO). NOAO is operated by AURA, Inc., under a cooperative agreement with the National Science Foundation.

REFERENCES

- Ajiki, M. et al. 2004, PASJ 56, 597
 Bertin, E. & Arnouts, S. 1996, A&AS, 117, 393
 Bruzual, G. & Charlot, S. 2003, MNRAS, 344, 1000
 Calzetti, D., Kinney, A. L. & Storchi-Bergmann, T. 1994, ApJ, 429, 582
 Charlot, S. & Fall, S. M. 1993, ApJ, 415, 580
 Cowie, L. L., & Hu, E. M. 1998, AJ, 115, 1319
 Dawson, S., Rhoads, J. E., Malhotra, S., Stern, D., Dey, A., Spinrad, H., Jannuzi, B. T., Wang, J. X. & Landes, E. 2004, ApJ, 617, 707
 Ellis, R., Santos, M. R., Kneib, J.-P. & Kuijken, K. 2001, ApJ, 560, L119
 Fujita, S. S. et al. 2003, ApJ, 586, L115
 Fukugita, M., Ichikawa, T., Gunn, J. E., Doi, M., Shimasaku, K. & Schneider, D. P. 1996, AJ, 111, 1748
 Fynbo, J. U., Möller, P. & Thomsen, B. 2001, A&A, 374, 443
 Gawiser, E. et al. 2006, /apj, 642, L13
 Hansen, M. & Oh, S. P. 2006, MNRAS, 367, 979
 Hu, E. M., Cowie, L. L. & McMahon, R. G. 1998, ApJ, 502, L99
 Hu, E. M., Cowie, L. L., McMahon, R. G., Capak, P., Iwamuro, F., Kneib, J.-P., Maihara, T. & Motohara, K. 2002, ApJ, 568, L75
 Hu, E. M., Cowie, L. L., Capak, P., McMahon, R. G., Hayashino, T. & Komiyama, Y. 2004, AJ, 127, 563
 Jannuzi, B. T., Dey, A. 1999, in ASP Conf. Ser. 191, Photometric Redshifts and High Redshift Galaxies, ed. R. J. Weymann, L. J. Storrie-Lombardi, M. Sawicki, & R. J. Brunner (San Francisco: ASP), 111

- Kodaira, K. et al. 2003, PASJ, 55, L17
 Kudritzki, R.-P. et al. 2000, ApJ, 536, 19
 Landolt, A. U. 1992, AJ, 104, 340
 Madau, P. 1995, ApJ, 441, 18
 Malhotra, S. & Rhoads, J. E. 2002, ApJ, 565, L71
 Malhotra, S., Wang, J.X., Rhoads, J. E., Heckman, T. M. & Norman, C. A. 2003, ApJ, 585, L25
 Malhotra, S. & Rhoads, J. E. 2004, ApJ, 617, L5
 McLeod, B. M., Caldwell, N., Williams, G. & Conroy, M. 2006, Megacam Observers Manual, http://grb.mmt.arizona.edu/~ggwilli/mmt/docs/megacam/megacam_observers_manual.html
 McLeod, B. A., Gauron, T. M., Geary, J. C., Ordway, M. P. & Roll, J. B. 1998, SPIE, 3355, 477
 Neufeld, D. A. 1991, ApJ, 370, L85
 Oke, J. B. & Gunn, J. E. 1983, ApJ, 266, 713
 Ouchi, M. et al. 2001, ApJ, 558, 83
 Ouchi, M. et al. 2003, ApJ, 582, 60
 Ouchi, M. et al. 2004, ApJ, 611, 685
 Papovich, C., Dickinson, M. & Ferguson, H. C. 2001, ApJ, 559, 620
 Partridge, R. B. & Peebles, P. J. E. 1967, ApJ, 147, 868
 Pentericci, L. et al. 2000, A&A, 361, 25
 Pirzkal, N. et al. 2004, ApJS, 154, 501
 Pirzkal, N. et al. 2007, in preparation
 Rhoads, J. E. 2000, PASP, 112, 771, 703
 Rhoads, J. E., Malhotra, S., Dey, A., Stern, D., Spinrad, H. & Jannuzi, B. T. 2000, ApJ, 545, L85
 Rhoads, J. E. & Malhotra, S. 2001, ApJ 563, L5
 Rhoads, J. E., Dey, A., Malhotra, S., Stern, D., Spinrad, H., Jannuzi, B. T., Dawson, S., Brown, M. J. I. & Landes, E. 2003, AJ, 125, 1006
 Rhoads, J. E., Xu, C., Dawson, S., Dey, A., Malhotra, S., Wang, J. X., Jannuzi, B. T., Spinrad, H., & Stern, D. 2004, ApJ, 611, 59
 Shimasaku, K. et al. 2003, ApJ, 586, L111
 Shimasaku, K. et al. 2006, PASJ, 58, 313
 Steidel, C. C., Giavalisco, M., Pettini, M., Dickinson, M. & Adelberger, K. L. 1996, ApJ, 462, L17
 Stiavelli, M., Scarlata, C., Panagia, N., Treu, T., Bertin, G. & Bertola, F. 2001, ApJ, 561, L37
 Taniguchi, Y. et al. 2005, PASJ, 57, 165
 Tody, D. 1993, ASPC, 52, 173
 Tody, D. 1986, SPIX, 627, 733
 Valdes, F. G. 1998, ASPC, 145, 53
 Valdes, F. G. & Tody, D. 1998, SPIE, 3355, 497
 Venemans, B. P. et al. 2002, ApJ, 569, L11
 Venemans, B. P. et al. 2004, A&A, 424, L17
 Wang, J. X., Rhoads, J. E., Malhotra, S., Dawson, S., Stern, D., Dey, A., Heckman, T. M., Norman, C. A. & Spinrad, H. 2004, ApJ, 608, L21
 Wang, J. X. et al. 2007, in preparation